JOURNAL OF SPACECRAFT AND ROCKETS
Vol. 47, No. 6, November–December 2010

High-Speed Spectrographic Photometry of the Stardust Sample Return Capsule Around Peak Deceleration

Hans C. Stenbaek-Nielsen*
University of Alaska, Fairbanks, Alaska 99775-7320
and
Peter Jenniskens
SETI Institute, Mountain View, California 94043

DOI: 10.2514/1.38476

The descent of the Stardust Sample Return Capsule on 15 January 2006 was observed with an intensified high-frame-rate slitless spectrograph, which was operated in staring mode. Spectra were recorded at 300 frames per second from 09:57:47 to 09:57:57 UTC (Coordinated Universal Time), around the time of peak deceleration of the capsule. At this time, the spectra contained continuum emission from the hot surface and appeared to be featureless otherwise, with the exception of the telluric absorption caused by molecular oxygen in the atmosphere between the capsule and the observer. By averaging all spectra together, however, it was possible to bring out weak emission lines of oxygen and potassium over the time frame 09:57:51–54 UTC and sodium emission during 09:57:48–51 UTC. The spectral sequence was analyzed for signs of variation in the total emission from a possible wobbling of the capsule at periods higher than the spin rate. No such variation was observed above the detection threshold of 5° amplitude in the line of sight.

I. Introduction

THE return of the Stardust Sample Return Capsule was the fastest ever attempted reentry of a spacecraft, with an entry speed of 12.8 km/s at 100 km altitude. The capsule was protected by an ablative heat shield that was flown for the first time. The shape of the capsule, center of gravity, spin rate, and attack angle (0 deg) were designed to have a purely ballistic (nonlifting) entry trajectory [1].

Leading up to the reentry, calculations were made of the expected trajectory, speed, and deceleration during descent, which revealed an aerodynamic instability in the high-altitude free-molecular regime [2,3]. That instability could lead to unacceptably large excursions in the angle of attack near peak heating and could result in mission failure. The uncertain behavior of the capsule added to the size of the landing ellipse at the Utah Test and Training Range. To reduce those excursions, the entry spin rate of the capsule was increased from an original 5 to 14–16 rotations per minute. The higher spin rate delayed the effect of the static instability, so that the Sample Return Capsule (SRC) traversed through the transitional regime from free-molecular flow to continuum flow without experiencing a large increase in the total angle of attack. Calculations predicted that the angle of attack pitched up to about 7 deg, before reducing to less than 2 deg during peak heating and peak dynamic pressure [2,3].

An airborne observing campaign was organized to observe this reentry with a range of spectrographic cameras, with a mission to observe the ablation and measure the surface temperature and amount of shock emission along the entry trajectory [4]. The altitude of the aircraft would provide low extinction and little scintillation from the atmosphere between capsule and observer. The reentry was nominal and was well observed by a wide range of instruments.

Here, we report on observations of the Stardust capsule reentry with an intensified high-frame-rate imager, which was set up in staring mode as a slitless spectrograph. This provided for very stable observing conditions, which permitted accurate photometry of the time variability of the capsule's radiation.

II. Instrument

Two instruments were deployed onboard NASA's DC-8 Airborne Laboratory [5] to measure short variations of capsule emissions, both operated from the same mount (Fig. 1). One was a high-speed 100,000 Hz photometer filtered at 391 nm on the peak of the N_2^+ emission band, with a 0.5° field of view (Fig. 1, top cylinder). The other was an intensified high-frame-rate charge-coupled-device (CCD) camera, operated at 300 frames per second.

Both were fixed mounted in a coaligned fashion toward a pointing elevation of about 21°, on a specially designed mount built by M & O Precision Machining. The mount was placed on a low equipment rack. The control hardware was mounted on a high rack outside the field of view of Fig. 1.

This camera was operated behind experimenter port 610L, equipped with a flat Pyrex window (no. SN84) [4]. The transmission properties of the window were measured in the laboratory. The window transmittance is essentially gray over the wavelength sensitivity range of the camera.

The camera was equipped with a Delft Instruments 105 mm $f0.7$ Raystar lens and a large-diameter blazed 230 lines/mm transmission grating placed in front of the lens, for a dispersion of 0.769 nm/pixel in second order. The detector consisted of 256×256 square pixels of 45 μm size with 256 gray levels (8 bits) and $6.25 \times 6.25°$ field of view. The intensifier is sensitive to light in the wavelength range from 500 to 900 nm, with a peak sensitivity at 700 nm. The gain is affected by the total scene brightness in a way that is not easy to quantify. The intensifier phosphor has a decay time constant of 0.8 ms, and hence afterglow is minimized [6].

Images were recorded in two hardware buffers each with storage for 4096 images. The switch between buffers required the camera to be off recording mode for 5–8 s. We elected to observe at 300 frames per second, yielding two 13 s image sequences that we planned for just before and after peak heating.

III. Observations

The observations were only partially successful due to operational errors. The high-speed photometer obtained no data, but the high-

---

Received 9 May 2008; revision received 12 April 2010; accepted for publication 12 April 2010.

*Geophysical Institute, 903 Koyukuk Drive; hnielsen@gi.alaska.edu (Corresponding Author).

Fig. 1 IHFRI as mounted in NASA's DC-8 Airborne Laboratory. The top cylinder is the mount for a photomultiplier tube, and the bottom assembly shows the grating, lens, intensifier, and CCD camera, respectively.

speed intensified imaging spectrograph recorded spectrographic data past the point of peak heating. The high-speed photometer was shut off during aircraft turns to prevent damage from light sources on the ground, but did not come back on during the actual Stardust SRC entry. The grating orientation on the high-speed intensified imaging spectrograph was slightly off the actual Stardust SRC entry path, so that the spectra were not projected on the imaging plane. Fortunately, the second sequence of data (after peak heating) was perfectly recorded.

Figure 2 shows examples of the recorded images. The grating dispersion direction was tilted at an angle aligned along the path of the Stardust Sample Return Capsule in projection on the sky. When the capsule passed through the camera field of view around the time of peak heating, it was too bright for the intensifier. The successful second observing sequence was started when the capsule had left the field of view toward the right. First, the first-order spectrum moved through the field of view, followed by the second- and third-order spectra, respectively, when the capsule continued to move further away from boresight.

The first frame of that second sequence (no. 032), shown in Fig. 2, was taken at 09:57:47 UTC (Coordinated Universal Time) and shows the mostly saturated first-order spectrum. Around frame no. 300 (09:57:48 UTC), the second-order spectrum came into view and this order was perfectly exposed. The second-order spectrum continued to move through the field of view (e.g., no. 680 in Fig. 2) and left the field around frame no. 2932 (09:57:56.7 UTC). After that, a faint third-order spectrum was recorded until around frame no. 3250 (09:57:57.8 UTC), when it rapidly faded because the capsule moved behind the edge of the window frame.

The width of each spectrum is determined by the instrument point spread function (a function of optical geometry and detector properties), not by the spatial dispersion of flux at the location of the capsule. At a range of 74 km (Table 1), an ideal instrument would have a maximum spatial resolution of only 32 m/pixel. The instrument point spread function has a full-width-at-half-maximum of about 2.3 pixels, for a maximum spatial resolution of 74 m, much larger than the diameter of the capsule.

During the observation of the first- and second-order spectra between 09:57:47 and 09:57:57 UTC, the SRC descended from 51.7 to 47.1 km altitude and moved from 40.631N, 244.729E to 40.520N, 245.360E at a speed from 7.1 to 4.5 km/s relative to the atmosphere (Table 1). The capsule had passed boresight and moved at 1.9 to 3.0°/s in azimuth and +0.8 to +0.6°/s in elevation. The viewing geometry was such that the capsule was seen progressively more from the back (frontal view of Surface viewing angle in Table 1 would be 0°), lowering the projected frontal surface area of the capsule from $0.515\ \mathrm{m}^2$ down to $0.259\ \mathrm{m}^2$.

A. Temporal Variation

At first sight, the spectra contain only continuum radiation, with the exception of a noticeable absorption band from molecular oxygen at 760 nm. At the time of the observation, shock emissions were no longer detected by other instruments [7,8].

The spectra were extracted along the main dispersion direction, by summing the total column intensity over a 9-pixel wideband centered on the spectrum, which is four times the full-width/half-maximum of the instrument's point spread function, so that all light is included. Figure 3 shows the sum pixel intensity for each frame between frame nos. 32 and 2932. The frame-to-frame scatter in the pixel intensity is only 2.6% (1 sigma) at the peak of the second-order spectrum passage. No obvious short-term variations in the signal are observed on a scale of 1–100 Hz.

B. Spectral Features

The individual spectra were extracted by rotating each spectrum and summing over a band ±4 pixels perpendicular to the dispersion direction. Rotation slightly changed the dispersion to 0.764 nm/pixel.

We searched for spectral emission lines in the second-order spectrum by averaging all uncalibrated spectra together (Fig. 4), allowing for the changing position of the spectrum on the CCD. The telluric absorptions from molecular oxygen (marked O_2-A and O_2-B in Fig. 4) were used to verify that the spectra were correctly aligned.

The wavelength scale of the spectrum does not significantly change while the second order glides by. We optimized the contrast in the sodium line emission by adopting a (very small) linear change in the rate of drift. Because so many spectra were recorded at good signal-to-noise S/N ratios, the average spectrum has about $S/N = 550$ (1 sigma) at 560 nm.

The wavelength scale was calibrated by using the wavelength of the oxygen A-band absorption, combined with the instrument

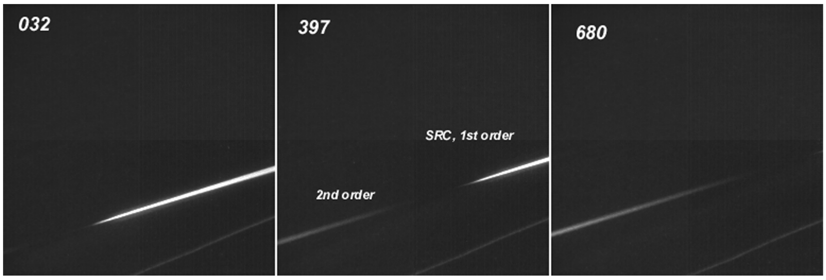

Fig. 2 Three typical images recorded at 09:57:47–48 UTC. The capsule was just outside the field of view to the right, moving further to the right. The spectrum created by the transmission grating moved from left to right in subsequent frames (first order is the bright part, followed by the fainter second order). A star is responsible for the faint spectrum at the bottom, oriented slightly differently.

Table 1 Change of viewing conditions and capsule orientation and position during the observations (after TMC-19 trajectory)

UTC time	Time from entry, s	Frame	Altitude, km	Velocity, km/s	Range, km	Azimuth, °	Angle from boresight, °	Elevation, °	Surface viewing angle, °	Projected surface area, m^2
09:57:47	64.7	0	51.7	7.1	111.3	279.5	+18.5	20.4	37.8	0.407
09:57:48	65.7	300	51.1	6.8	105.9	281.5	+20.5	21.3	39.9	0.395
09:57:49	66.7	600	50.6	6.5	100.9	283.6	+22.6	22.1	42.1	0.382
09:57:50	67.7	900	50.1	6.3	96.3	285.9	+24.9	23.0	44.4	0.368
09:57:51	68.7	1200	49.6	6.0	92.0	288.5	+27.5	23.8	46.9	0.353
09:57:52	69.7	1500	49.2	5.7	88.1	291.2	+30.2	24.6	49.4	0.338
09:57:53	70.7	1800	48.7	5.5	84.6	293.7	+32.7	25.4	52.0	0.321
09:57:54	71.7	2100	48.3	5.2	81.4	296.4	+35.4	26.2	54.6	0.304
09:57:55	72.7	2400	47.9	5.0	78.5	299.4	+38.4	27.0	57.4	0.286
09:57:56	73.7	2700	47.5	4.8	75.9	302.5	+41.5	27.6	60.2	0.268
09:57:57	74.7	3000	47.1	4.5	73.7	305.5	+44.5	28.3	63.0	0.250
09:57:58	75.7	3300	46.8	4.3	71.7	308.7	+47.7	28.8	65.8	0.232

sensitivity dropoff at short wavelengths in first and second order, even without knowing the exact wavelength of this dropoff, but knowing that this wavelength in second order is twice that in first order. Following the identification of the sodium and potassium lines, the scale was further refined from the position of these observed atomic emission lines.

A weak 777 nm oxygen line (marked O in Fig. 4) was detected between 09:57:51, when the relevant spectral range in second order first entered the field of view, until 09:57:53 UTC. This late in flight, no air plasma emissions were detected by other instruments.

We also detected potassium emission (labeled K) in spectra taken in this same time interval, but those lines continued to be present until the relevant spectral range exited the field of view.

Sodium emission (labeled Na) was detected in spectra taken from 09:57:48 to 09:57:51 UTC, when the relevant spectral range was in view. The phenol-impregnated carbon ablator released carbon and hydrogen atoms, which reacted with the atmosphere to form CN. However, no hydrogen alpha emission was detected at 656 nm. Our instrument is not sensitive around 388 nm in the range where CN emits, nor above 900 nm, where carbon atom lines have been detected by other instruments [8].

C. Absolute Calibration of Line Intensities

The absolute calibration of the spectra involved understanding the instrument response for different incident angles. Figure 5 shows the average spectra extracted over periods of 1 s (300 frames each), starting at frame no. 032. Subsequent spectra are shown in an alternating sequence of solid and dashed lines. The wavelength scale pertains to the second-order spectrum. The first-order spectrum is to the right, and a faint contribution from the third-order spectrum is visible to the left.

It is clear from this graph that the response curve of the instrument is not only a function of wavelength, but also a function of the incident angle of the light, which changed when the position of the source in the sky changed. There may also be a dependence on pixel position in the camera, if there was any form of vignetting in the optical pathway. The high-pixel part of each spectrum traces a contour that appears to define the wavelength-dependent response from the sensitivity of the CCD camera. However, each individual spectrum is underrepresented at the lower two thirds of pixel positions. Also, individual spectra show wiggles that may be caused by unfavorable properties of the CCD detector or by thin-film interference in the line of sight. Fortunately, those wiggles tend to average out when the source moves across the field of view (e.g., compare Figs. 4 and 5).

These effects were unknown to us during the observing campaign and no calibrations were made at the time to permit us to correct for this now.

One way to obtain absolutely calibrated line intensities is to scale the reduced spectra to the flux inferred from other instruments. The spectra are dominated by continuum emission. It was assumed that instrumental effects scale the continuum radiation (of less interest here) and the line radiation in the same manner, and that the continuum radiation is well represented by a graybody of a given temperature.

We first corrected the individual spectra (1 s averages) for the instrument response derived from the average spectrum over the full time series, and then correcting individual spectra for the

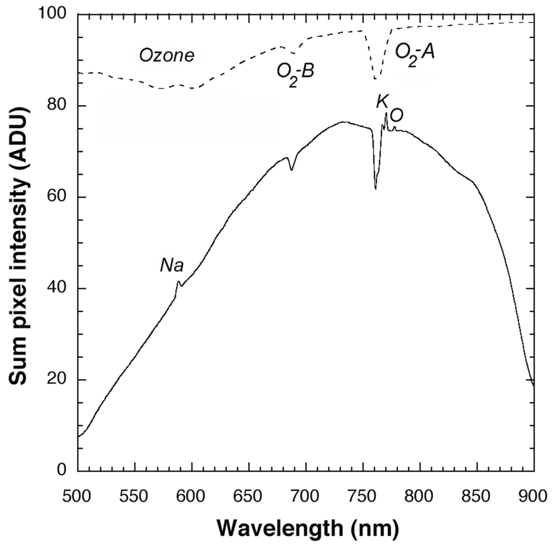

Fig. 4 Average spectrum over time span 09:57:49–56 UTC. Also shown is the telluric extinction (in percent transmittance, same scale) for an altitude of 50 km and elevation of 20° (ModTran).

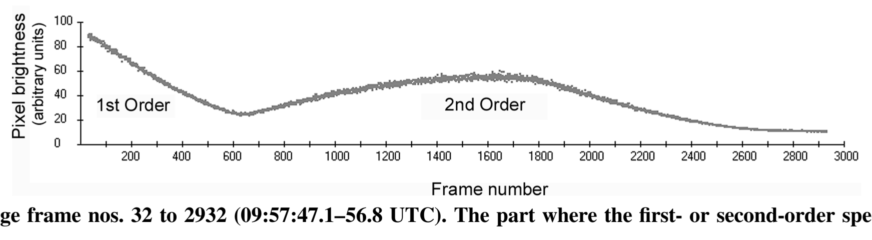

Fig. 3 Brightness in image frame nos. 32 to 2932 (09:57:47.1–56.8 UTC). The part where the first- or second-order spectrum dominates the total emission is indicated.

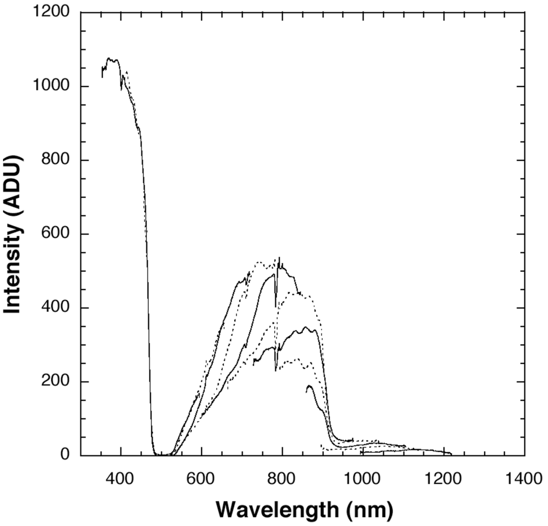

Fig. 5 Extracted spectra for periods of 1 s intervals. Subsequent extractions of frames are shown in an alternating sequence of solid and dashed lines.

angle-dependent effects shown in Fig. 5. The result matched the expected continuum emission of a blackbody, leaving sinusoidal residues of order ±5%. The uncertainty in the absolute flux measured by other instruments is of order 10% [8,9]. Hence, the uncertainty in the absolute flux of the emission lines is mostly determined by how well the continuum flux was measured by these other instruments.

The flux at 548 nm has been measured by the digital imager (DIM) instrument [9] and the 930–1075 nm flux by near-infrared spectrograph (NIRSPEC) [8], from which the mean capsule's surface temperature was measured, using the range and projected surface area of the capsule. The scaling factor of 0.185, which includes the emissivity ~0.88, was kept constant. From 09:57:48.5 to 09:57:53.5, the best-fit graybody temperatures decreased from 2750 K to 2620, 2480, 2340, 2260, and 2170 K (±20 K). The surface cooled at an average rate of 118 K/s. The corresponding continuum flux profiles are shown by a dashed line in Fig. 6. The continuum of each intensified high-frame-rate imager (IHFRI) camera spectrum was subsequently matched to these profiles.

The reported flux in Fig. 6 is that measured just outside the aircraft after correction for extinction between capsule and observer, but leaving the telluric O_2 absorption bands in place. Imperfect removal of those bands might have affected the potassium line strength.

It is evident that the oxygen line continued to decrease in intensity relative to the continuum emission during this late part of the entry trajectory, more rapidly than that of the potassium and sodium lines.

IV. Discussion

The potassium and sodium line emission cannot have originated from potassium and sodium atoms in the atmosphere, which are rare at altitudes of 54–48 km, and therefore must have originated from material ablated by the thermal protection system. At this time, it is not clear whether the sodium and potassium atoms are impurities in the PICA (phenol-impregnated carbon ablator) material or originated from residual paint at the edge of the heat shield. A white paint layer was applied for thermal control, and both sodium and potassium were detected when this paint layer ablated early during descent [7]. Photographs of the recovered capsule show residues of this white paint on the back shell of the heat shield.

The lack of atemporal variation of continuum flux at frequencies of 1–100 Hz raises the question whether such variations might have been expected.

During the entry, the capsule aerodynamically decelerated from ~12.8 km/s to subsonic speeds. Figure 7 shows the calculated deceleration of the capsule [10] (solid line) and the reconstructed deceleration (dashed line) from astrometric observations of the reentry [11]. The latter is at lower temporal resolution than the calculations and the reconstructed trajectory does not show the effects from possible wobbling of the capsule. The reconstructed trajectory has a peak deceleration of 0.32 km/s^2 and was higher than 0.2 km/s^2 between 09:57:33 and 09:57:58 UTC, as predicted, following the point of peak heating around 09:57:33 UTC. The calculated deceleration varied around this mean with periods of about 1.2–2.6 s (Fig. 7).

Such oscillations can derive from instabilities in the capsule's orientation, which immediately lead to periodic variations in shock emission line intensity (with changing attack angle) and in the strength of continuum emission (from a changing view of the projected surface area of the hot capsule).

The oxygen 777 nm shock emission line was too weak for us to measure independently over a long enough time sequence to determine such variability (Fig. 6).

The continuum emission, on the other hand, was observed for a period of about 10 s. Because the capsule passed by the observer at that time, the effective surface area was decreasing at a rate of 0.006 m^2 per degree of change in viewing angle (Table 1). That is between 1.5 and 2.5% of the total surface area at any given time. Hence, a small 1° wobble in the orientation of the capsule along the line of sight would have caused a ~2% peak-to-peak variation in the measured continuum flux.

The data sample of Fig. 3 covers about 9.7 s, or just over two spinning cycles of the spacecraft and of order five possible wobble periods. Unfortunately, the variations due to the response of the instrument mask the variations expected from a spacecraft wobble. The data suggest that this wobble resulted in less than 10% peak-to-peak variation in flux, corresponding to a smaller than 5° wobble in the line of sight.

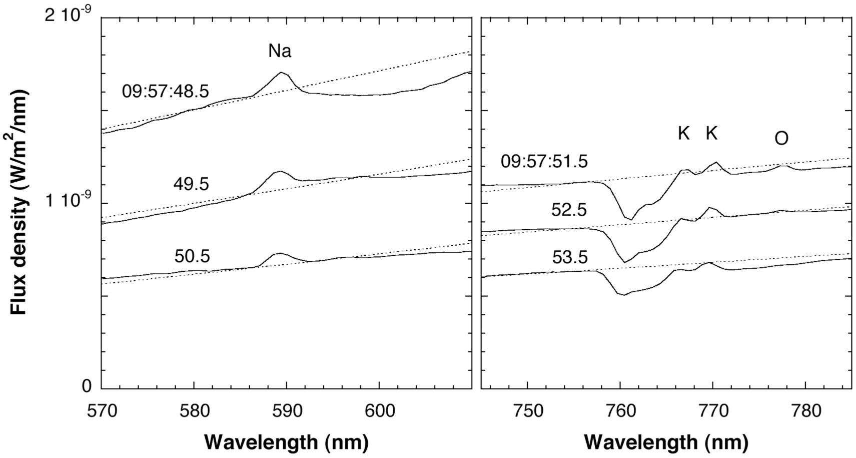

Fig. 6 Fully reduced spectra (apparent flux at aircraft window, corrected for extinction but not for oxygen *A*-band absorption) for period when Na, K, and O lines were detected. Dashed lines are graybody profiles fitted to calibrated broadband 548 nm and 930–1075 nm flux data [8,9].

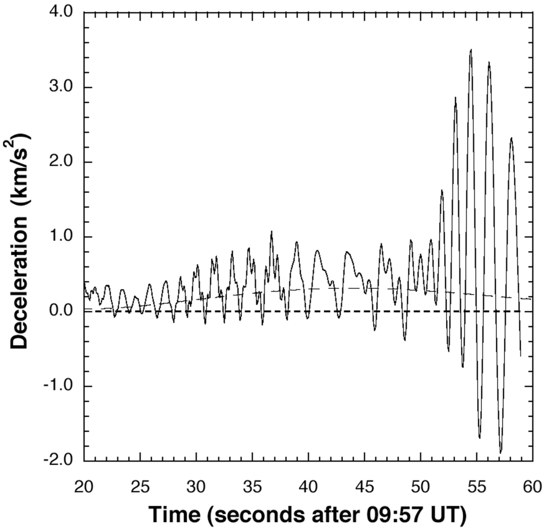

Fig. 7 Calculated (solid line) and reconstructed (dashed line) deceleration of the Stardust Sample Return Capsule during entry on 15 January 2006.

V. Future Work

The results are available now for interpretation. The strength of the observed oxygen line emission may be especially useful to validate radiative flow models of shock emission deeper down in the Earth's atmosphere. If the sodium and potassium impurities are from the PICA material itself, then the sodium and potassium emissions may provide insight into the ablation rate of the PICA around peak deceleration.

The observations of the Stardust Sample Return Capsule entry are expected to remain a unique system field test for a long time to come. The observational data and the calibration files will be archived for this purpose. The present paper serves to document the files in hand.

VI. Conclusions

An intensified high-frame-rate spectrographic camera captured spectra of the Stardust Sample Return Capsule at a rate of 300 frames per second during the period 09:57:47 and 09:57:57 UTC. During a significant fraction of this time frame, the second-order spectrum is perfectly exposed close to the center of the field of view. The staring mode of operation, and the lack of atmospheric scintillation, provide for a good signal-to-noise ratio of only 2.6% frame-to-frame standard deviation. No significant periodic variation in the signal strength is observed during this time interval at frequencies above the capsule's spin rate and below 100 Hz. A wobble, if any, was less than the detection threshold of 5° amplitude in the line of sight. Averaging of all second-order spectra reveal the presence of weak lines of sodium, potassium, and oxygen.

Acknowledgments

This work was funded and managed by the Orion Thermal Protection System Advanced Development Project and the NASA Engineering and Safety Center. NASA's DC-8 Airborne Laboratory was deployed by the University of North Dakota and National Suborbital Education and Research Center under contract with NASA Wallops Flight Center. We thank Takeshi Kammae for helping install and test the camera. Haiping Su of the Airborne Science and Technology Laboratory at NASA Ames Research Center performed the ModTran calculations of atmospheric extinction. Calculations of expected emission levels by Mike Wright and Joe Olejniczak at NASA Ames Research Center made it possible for us to set the instrument settings correctly. Dave E. Jordan of NASA Ames Research Center acted as the NASA Program Manager for the mission and designed methods for instrument installation. Jeff Ignaitis from M & O Precision Machining designed and built the instrument's mounting hardware.

References

[1] Desai, P. N., Braun, R. D., Engelund, W. C., Cheatwood, F. M., and Kangas, J. A., "Mars Ascent Vehicle Flight Analysis," 7th AIAA/ ASME Joint Thermodynamics and Heat Transfer Conference, Albuquerque, NM, AIAA Paper 98-2850, June 1998.

[2] Desai, P. N., Mitcheltree, R. A., and Cheatwood, F. M., "Entry Dispersion Analysis for the Stardust Comet Sample Return Capsule," *Journal of Spacecraft and Rockets*, Vol. 36, No. 3, 1999, pp. 463–469. doi:10.2514/2.3467

[3] Desai, P. N., Mitcheltree, R. A., and Cheatwood, F. M., "Entry Trajectory Issues for the Stardust Sample Return Capsule," *International Symposium on Atmospheric Reentry Vehicles and Systems*, Arcachon, France, Paper 15.1, March 1999.

[4] Jenniskens, P., Kontinos, D., Jordan, D., Wright, M., Olejniczak, J., Raiche, G., et al., "Preparing for the meteoric return of Stardust," *Dust in Planetary Systems*, edited by A. Grapps and E. Gruen, ESA, SP 643, Paris, 2006.

[5] *DC-8 Experimenters Hand Book*, NASA Dryden Flight Research Center, 2003.

[6] Stenbaek-Nielsen, H. C., and Jenniskens, P., "Leonid at 1000 Frames per Second," *Institute of Space and Astronautical Science Report*, SP 15, 2003, pp. 207–214.

[7] Jenniskens, P., "Observations of the Stardust Sample Return Capsule Entry with a Slit-Less Echelle Spectrograph," *Journal of Spacecraft and Rockets*, Vol. 47, No. 5, 2010, pp. 718–735. doi:10.2514/1.37518

[8] Taylor, M., and Jenniskens, P., "Near-IR Spectroscopy of the Stardust Sample Return Capsule Entry: Detection of Carbon,"*Journal of Spacecraft and Rockets*, Vol. 47, No. 6, 2010, pp. 878–883. doi:10.2514/1.38075

[9] Jenniskens, P., and Wercinski, P. F., "Digital Still Snapshots of the Stardust Sample Return Capsule Entry,"*Journal of Spacecraft and Rockets*, Vol. 47, No. 6, 2010, pp. 873–877. doi:10.2514/38074

[10] Desai, P. N., and Qualls, G., "Stardust Entry Reconstruction," 46th AIAA Aerospace Sciences Meeting and Exhibit in Reno, NV, AIAA Paper 2008-1198, Jan. 2008.

[11] Levit, C., Albers, J., Jenniskens, P., and Spurny, P., "Reconstruction and Verification of the Stardust SRC Re-Entry Trajectory," 46th AIAA Aerospace Sciences Meeting and Exhibit in Reno, NV, AIAA Paper 2008-1199, Jan. 2008.

D. Kontinos
Guest Editor